

# Gasdermin E-dependent and -independent Subroutines Regulate the Passage of Dextrans During Apoptosis-driven Secondary Necrosis.

**Elke De Schutter**

VIB-UGent Center for Inflammation Research: VIB-UGent Inflammatie-researchcentrum

**Jana Ramon**

Ghent University: Universiteit Gent

**Benjamin Pfeuty**

University of Lille: Universite de Lille

**Caroline De Tender**

Ghent University: Universiteit Gent

**Stephan Stremersch**

Ghent University: Universiteit Gent

**Koen Raemdonck**

Ghent University: Universiteit Gent

**Ken Op de Beeck**

University of Antwerp: Universiteit Antwerpen

**Wim Declercq**

VIB-UGent Center for Inflammation Research: VIB-UGent Inflammatie-researchcentrum

**Franck B. Riquet**

VIB-UGent Center for Inflammation Research: VIB-UGent Inflammatie-researchcentrum

**Kevin Braeckmans**

Ghent University: Universiteit Gent

**Peter Vandenabeele** (✉ [Peter.Vandenabeele@irc.vib-ugent.be](mailto:Peter.Vandenabeele@irc.vib-ugent.be))

VIB-UGent Center for Inflammation Research: VIB-UGent Inflammatie-researchcentrum

<https://orcid.org/0000-0002-6669-8822>

---

## Research Article

**Keywords:** Gasdermin E, Apoptosis, Secondary necrosis, Cell death, Membrane permeabilization, Efflux, Influx, Dextran

**Posted Date:** June 18th, 2021

**DOI:** <https://doi.org/10.21203/rs.3.rs-592826/v1>

**License:**  This work is licensed under a Creative Commons Attribution 4.0 International License.

[Read Full License](#)

---

# Abstract

Secondary necrosis has long been perceived as an uncontrolled process resulting in total lysis of the apoptotic cell. Recently, it was shown that progression of apoptosis to secondary necrosis is regulated by Gasdermin E (GSDME), which requires activation by caspase-3. Although the contribution of GSDME in this context has been attributed to its pore-forming capacity, little is known about the kinetics and size characteristics of this. Here we report on the membrane permeabilizing features of GSDME by monitoring the influx and efflux of dextrans of different sizes into/from anti-Fas stimulated L929sAhFas cells undergoing apoptosis-driven secondary necrosis. We found that GSDME accelerates cell lysis measured by SYTOX Blue staining but does not affect the exposure of phosphatidylserine on the plasma membrane. Furthermore, loss of GSDME expression clearly hampered the influx of fluorescently labeled dextrans while the efflux happened independent of the presence or absence of GSDME expression. Importantly, both in- and efflux of dextrans was dependent on their molecular weight. Altogether, our results demonstrate that GSDME regulates the passage of compounds together with other plasma membrane destabilizing subroutines.

## Introduction

Apoptosis, the best-known form of regulated cell death, is essentially a containment and recycling program that prepares the cell corpse for efficient phagocytosis [1]. However, when phagocytes are absent or the phagocytic capacity is insufficient, apoptotic cells progress to necrotic plasma membrane permeabilization called apoptosis-driven secondary necrosis, which results in a more inflammatory environment [2–5]. The gasdermin (GSDM) protein family gained a lot of interest as plasma membrane permeabilizers during regulated cell death [6–13]. Gasdermin D (GSDMD) is proteolytically activated by caspase-1 and -4 leading to inflammasome-mediated pyroptosis [7, 14] and the GSDMD-dependent release of pro-inflammatory cytokines such as interleukin-1 $\beta$  [15]. Similarly, apoptosis-driven secondary necrosis is driven by the activation of gasdermin E (GSDME) [9, 10]. To entail its effect, caspase-3-mediated cleavage induces the release of GSDME's cytotoxic N-terminal p30 fragment from the auto-inhibiting C-terminal domain, which is followed by plasma membrane recruitment and plasma membrane permeabilization [6, 9, 16]. Nevertheless, GSDME may not be the only mechanism responsible for secondary necrosis. GSDME expression is dispensable for secondary necrosis following NLR4-mediated apoptosis in macrophages [17] or UV irradiation-induced apoptosis in human T cells and monocytes [18].

The structure of GSDMD and the murine gasdermin A3 (GSDMA3) revealed a mechanism how the N-terminal domain is able to form pores [6, 19, 20]. Using cryo-electron microscopy, it was discovered that the N-terminal domains of GSDMA3 form a large, 27-fold  $\beta$ -barrel-shaped pore with an inner diameter of 18 nm [20]. In addition, 26- and 28-fold oligomerization structures were reported with similar dimensions as the dominant 27-subunit GSDMA3 pore [20]. In contrast, GSDMD oligomerization is reported to be more heterogeneous [6, 21, 22]. The N-terminal domain of GSDMD assembles into dynamic arc- and slit-shaped oligomers that finally transform to stable ring-shaped oligomers with varying diameters ranging from 13.5 till 33.5 nm [21, 22].

Unlike GSDMA3 and GSDMD, the characteristics of GSDME pore formation are currently unknown. Therefore, to gain insight in the membrane permeabilizing behavior of GSDME and its role in apoptosis-driven secondary necrosis, we applied two *in vitro* approaches. With the assumption that GSDME forms pores in the plasma membrane, influx or efflux of macromolecules, such as fluorescently labeled dextrans, is expected to happen when cells are exposed to apoptotic stimuli. Monitoring the uptake of fluorescently labeled dextrans in apoptotic cells is quite straightforward, only requiring the addition of the dextrans to the culture medium after apoptosis induction. However, monitoring efflux is less obvious as the cells should be pre-loaded with the dextrans in a manner that does not interfere with cellular processes such as proliferation or without inducing apoptosis by itself. Therefore, we selected nanoparticle-sensitized photoporation, which is an emerging intracellular delivery technique that enables direct cytosolic delivery of membrane-impermeable macromolecules in virtually every cell type with minimal impact on the cellular homeostasis [23–29]. This technique makes use of photothermal nanoparticles, like gold nanoparticles (AuNPs), which are incubated with cells and bind to the plasma membrane. Upon irradiation by a short, yet intense laser pulse, the AuNPs become heated, resulting in the evaporation of the surrounding water and the formation of quickly expanding water vapor nanobubbles (VNBs) around the AuNPs. The mechanical forces resulting from the expansion and collapse of those VNBs lead to the generation of localized pores in the plasma membrane [27, 30]. Through those transient plasma membrane pores, which are repaired within seconds to minutes, exchange of molecules between the intra- and extracellular compartment can happen [25, 26, 28, 29]. Importantly, under controlled conditions, complete cellular recovery is reported within 24 h upon laser treatment with minimal effect on the cellular homeostasis [23, 24, 26].

Here, we studied the membrane permeabilizing behavior of GSDME during apoptosis-driven secondary necrosis and attempted to elucidate whether this process is characterized by discrete pore sizes and/or whether GSDME pores grow over time. To this end, we developed GSDME-deficient L929sAhFas cells carrying a doxycycline-inducible system for GSDME expression allowing the exploration of secondary necrosis in the absence or presence of GSDME in the same cellular context. We reveal that absence of GSDME delays nuclear staining by SYTOX Blue (SB), as cells remain longer in the sublytic phase, while phosphatidylserine (PS) exposure was not affected. Next, we investigated the involvement of GSDME in the influx and efflux of fluorescently labeled dextrans of different sizes during apoptosis-driven secondary necrosis induced by anti-Fas. We provide evidence that pore formation during apoptosis-driven secondary necrosis is a gradual process that already supports a GSDME-dependent influx of fluorescently labeled dextrans before nuclear DNA of dying cells is stained by SB. Furthermore, the influx method allowed us to make an estimation of molecular sizes able to pass the GSDME pore. In contrast, efflux of fluorescently labeled dextrans seemed to occur independent of GSDME combined with the fact that only significant dextran loss was observed when cells were already stained by SB.

## Materials And Methods

### Cell Culture

L929sAhFas cells and derivatives were cultured in Dulbecco's Modified Eagle Medium supplemented with 10 % of Fetal Bovine Serum (v/v), L-glutamine (2 mM) and sodium pyruvate (400 mM). Cells were cultured in 37 °C in a humidified atmosphere containing 5 % CO<sub>2</sub> and were regularly tested against mycoplasma contamination.

### **Generation of gasdermin E-deficient L929sAhFas cells**

Single guide RNAs (sgRNA) targeting the exon 4 of *Gsdme* were selected using the the Wellcome Trust Sanger Institute Genome Editing database (WGE) [31] and were manufactured by Thermo Fischer Scientific. The sgRNA sequences are listed in Supplementary Table S1. The sgRNA oligo sequence was cloned in Bpil-digested pSpCas9(BB)-2A-GFP carrying *Streptococcus pyogenes* WT Cas9 (Addgene, plasmid no. 48138). The sgRNA Cas9 plasmid was transfected into L929sAhFas cells via jetPRIME transfection reagent (Polyplus-transfection). 4 µg plasmid was added per 25 000 cells and incubated for 4 h at 37 °C, 5 % CO<sub>2</sub>. After which the culture medium was replaced and cells were further incubated for 4 days at 37 °C, 5% CO<sub>2</sub>. Next, cells were harvested and GFP-positive cells were sorted using a FACSAria III (BD Biosciences). Effective genomic interruption of *Gsdme* was confirmed with PCR and Sanger sequencing. Allele editing was analyzed using TIDE [32]. The PCR and sequencing primers used are listed in Supplementary Table S1.

### **Generation of stable gasdermin E-inducible L929sAhFas cells line**

The L929sAhFas iGSDME cell line was obtained by transduction of *Gsdme* KOcl2 L929sAhFas cells with a pDG2-mGSDME-blast plasmid. This is a tetracycline-inducible derivative of pLenti6 (Life Technologies) containing a blasticidin selection marker [33], in which the coding sequence of murine GSDME was cloned. Upon lentiviral transduction, the stably transduced cells were selected with 5-10 µg/ml blasticidin.

### **Analysis of phosphatidylserine exposure and cell death kinetics**

L929sAhFas iGSDME cells were seeded in 24-well suspension plates (100 x 10<sup>3</sup> cells/well) in the presence or absence of doxycycline (Sigma-Aldrich, 1 µg/ml) and stimulated the next day with 125 ng/ml anti-Fas (clone CH11, Upstate). Cell death parameters were analyzed after incubation between 0 h and 10 h of anti-Fas treatment. 1 h before measurement, fluorescent probes were added to the culture medium: 1.25 µM of SYTOX Blue nucleic acid stain and 7.5 nM of annexin V Alexa Fluor 488 conjugate (Molecular Probes). Subsequently, samples were measured by flow cytometry using a four-laser BD Fortessa or three-laser BD LSR II (BD Biosciences) and data was analyzed using FlowJo 10.7.1.

### **Western Blotting**

L929sAhFas iGSDME cells were pretreated with 1 µg/ml doxycycline (Sigma-Aldrich) to allow GSDME expression. L929sAhFas and L929sAhFas iGSDME cells were incubated for 8 h with 250 ng/ml anti-Fas (clone CH11, Upstate) at 37 °C, 5 % CO<sub>2</sub>. (clone CH11, Upstate), after which they were harvested and washed twice in ice-cold phosphate-buffered saline (PBS). Next, cells were lysed using ice-cold RIPA lysis

buffer (50 mM Tris-HCl; pH 7.5; 150 mM NaCl; 1 mM EDTA; 0.5% sodium deoxycholate; 1 % Triton X-100 and 0.1 % SDS) freshly supplemented with EDTA-free complete protease inhibitor cocktail tablets and phosphatase inhibitor cocktail tablets (Roche Diagnostics Belgium N.V.). Extracted proteins were separated on 12 % sodiumdodecylsulfate (SDS) polyacrylamide gels and transferred onto nitrocellulose membranes (Amersham Bioscience). Membranes were blocked using tris-buffered saline containing 0.05 % Tween<sup>®</sup> 20 (TBS-T) and 5 % non-fat dry milk (Biorad) followed by incubation with anti-GSDME (ab215191, abcam) or anti-actin (69100, MP Biomedicals). After incubation with the horseradish peroxidase (HRP)-linked donkey anti-rabbit IgG or HRP-linked sheep anti-mouse (Amersham Biosciences), blots were revealed using a Western Lightning Plus-ECL (PerkinElmer).

### **Intracellular delivery of FITC-labeled dextrans by nanoparticle-sensitized photoporation**

AuNPs with a core size of 60 nm were in-house synthesized using the Turkevich method and coated with the cationic polymer poly(diallyl dimethyl ammonium chloride) (PDDAC) as reported before [23].

To determine the AuNP concentration that provides optimal photoporation results, L929sAhFas ( $130 \times 10^3$ ) were seeded in 24-well plates and allowed to attach overnight at 37 °C, 5 % CO<sub>2</sub>. Next, cells were incubated for 30 min (37 °C, 5 % CO<sub>2</sub>) with different concentrations of AuNPs (2, 4, 6, 8 and  $16 \times 10^7$  AuNPs/mL), washed with PBS to remove unbound AuNPs, and replenished with fresh culture medium containing 5 mg/ml FITC-labeled dextran (Sigma-Aldrich) of 10 kDa (FD10). Subsequently, cells were photoporated using an in-house built laser irradiation set-up equipped with a nanosecond pulsed laser (5 ns pulse duration,  $\lambda = 532$  nm, Tor, Cobolt) and a galvano scanner (Thorlabs, THORLABS-GVS002.SLDPRT) for rapid beam scanning across the samples. A fixed laser pulse fluence (optical energy per unit area) of 1.6 J/cm<sup>2</sup> was applied. After laser treatment, FD10-diluted medium was removed and cells were washed twice with culture medium and once with PBS followed by cell detachment using 0.25% trypsin-EDTA. At last, cells were measured for their FD10 content by flow cytometry using a three-laser BD LSR II (BD biosciences) and data was analyzed using FlowJo 10.7.1.

For loading with FITC-labeled dextrans in function of efflux experiments, L929sAhFas iGSDME cells ( $650 \times 10^3$  cells/well) were seeded in a 6-well plate and allowed to attach overnight at 37 °C, 5 % CO<sub>2</sub>. The same protocol as described before was used. In this case, cells were incubated with the optimal AuNP concentration ( $6 \times 10^7$  AuNPs/mL) for 30 min. After washing away of unbound AuNPs, culture medium was added containing FITC-labeled dextrans (Sigma-Aldrich) of 4 kDa (FD4), 10 kDa (FD10), 40 kDa (FD40), 70 kDa (FD70), 150 kDa (FD150), 250 kDa (FD250), 500 kDa (FD500) or 2000 kDa (FD2000). For all sizes a concentration of 5 mg/ml was used, except for 2000 kDa for which the concentration was increased to 10 mg/ml. Cells were subsequently photoporated using a fixed laser pulse fluence of 1.6 J/cm<sup>2</sup> after which the dextran-containing medium was removed and cells were washed twice with culture medium. After 2 h of incubation (37 °C and 5 % CO<sub>2</sub>), the same procedure was repeated a second time to further increase the percentage of fluorescently labeled cells. Finally, cells were detached using trypsin-

EDTA and re-seeded at  $100 \times 10^3$  cells/well in 24-well suspension plates in the presence or absence of doxycycline (Sigma-Aldrich, 1  $\mu\text{g}/\text{ml}$ ) and allowed to grow overnight (37 °C, 5 %  $\text{CO}_2$ ).

### **Influx and efflux of fluorescently labeled dextrans and cell death analysis**

For influx experiments, L929sAhFas iGSDME cells were seeded in 24-well suspension plates ( $100 \times 10^3$  cells/well) in the presence or absence of doxycycline (Sigma-Aldrich, 1  $\mu\text{g}/\text{ml}$ ) and treated the next day with 250 ng/ml anti-Fas (clone CH11, Upstate) for 10 h every 2 h. Afterwards, cells were harvested by gently pipetting up and down and were immediately centrifuged at 400 g for 5 min at 4 °C. After removing the supernatant, the cells were resuspended in culture medium containing 0.5 mg/ml Texas Red-labeled dextran (Thermofisher Scientific and Nanocs) of 10 kDa (TR10), 40 kDa (TR40), 70 kDa (TR70) or 2000 kDa (TR2000) and incubated for 5 min at room temperature. Next, cells were centrifuged again for 5 min at 400 g and 4 °C, washed and resuspended in culture medium containing 2.5  $\mu\text{M}$  SYTOX Blue (Molecular Probes) for nuclear staining. Samples were subsequently measured by flow cytometry using a four-laser BD Fortessa (BD Biosciences) and data was analyzed using FlowJo 10.7.1.

For efflux experiments, L929sAhFas iGSDME cells were preloaded with FITC-labeled dextrans (Sigma-Aldrich) using nanoparticle-sensitized photoporation and re-seeded in 24-well suspension plates in the presence or absence of doxycycline (Sigma-Aldrich, 1  $\mu\text{g}/\text{ml}$ ). One day after photoporation, re-seeded L929sAhFas iGSDME were treated with 250 ng/ml anti-Fas (clone CH11, Upstate) for 10 h every 2 h. Subsequently, cells were stained with SYTOX blue (Molecular probes) at a concentration of 2.5  $\mu\text{M}$  after which they were collected by gently pipetting up and down and measured by flow cytometry using a three-laser BD LSR II (BD Biosciences). Data was analyzed using FlowJo 10.7.1.

### **CellTiter-Glo<sup>®</sup> cell viability assay**

In view of determining the optimal AuNP concentration, cell viability was assessed 2 h post laser treatment using the CellTiter-Glo<sup>®</sup> luminescent cell viability assay (Promega) following the manufacturer's protocol. Briefly, culture medium was replaced by equal amounts of fresh culture medium and CellTiter-Glo<sup>®</sup> reagents and cells were mixed for 30 min using an orbital shaker at 120 rpm. After allowing stabilization of the luminescent signal for 15 min, equal volumes of each well were transferred to an opaque well plate and luminescence was recorded by a Glomax Luminometer (Promega).

### **Statistical analysis**

Results are presented as means  $\pm$  SD. Statistical analysis of PS exposure and SB staining in function of time were performed using PRISM 8 software (GraphPad) using a two-way ANOVA with the Geisser-Greenhouse correction (matched values were stacked into a subcolumn). For the influx and efflux dataset, homogeneity of variances and data normality were checked graphically (boxplots, QQPlots respectively). Analysis of the influx of Texas Red-labeled dextrans was done making use of a generalized linear model (GLM), poisson family. To study the effect of dextran size on either the SB-negative (SB-) and SB-positive (SB+) cells, the factor variables doxycycline addition and measured point in time (0, 2, 4, 6, 8 and 10 h of

anti-Fas treatment) and the discrete variable dextran size were included in the model. To study the effect of doxycycline on the influx of Texas Red-labeled dextrans, doxycycline addition, the measured point in time (0, 2, 4, 6, 8 and 10 h of anti-Fas treatment) and dextran size were all set as factor variables in the GLM. Multiple comparisons were made making use of the package “multcomp” [34].

To analyze the efflux of FITC-labeled dextrans, the dataset was split in three populations (SB-, SB low+, SB high+). For both datasets, a GLM (Gaussian family) was fitted to study the effect of dextran size and doxycycline on the efflux of dextrans. The factor variables doxycycline, measured point in time (0, 2, 4, 6, 8 and 10 h of anti-Fas treatment) and the discrete variable dextran size were included in the model. Again, multiple comparisons were made using the package “multcomp”. All analysis were done in R, version 4.3 on three biological replicates of each data-set [35].

Differences with a p-value < 0.05 were considered significant and indicated as followed: ns = nonsignificant; \* p < 0.05; \*\* p < 0.01; \*\*\* p < 0.001.

## Results

### **Gasdermin E accelerates plasma membrane permeabilization during apoptosis-driven secondary necrosis as measured by SYTOX Blue-mediated nuclear staining.**

As conflicting findings were reported on the contribution of GSDME to apoptosis-driven secondary necrosis [9, 10, 17, 18], we decided to investigate the GSDME function in the murine fibrosarcoma cell line L929 stably expressing the human Fas receptor (L929sAhFas). Treatment of L929sAhFas cells with agonistic anti-Fas antibody induces apoptosis and caspase-3 activation via the caspase-8-dependent proteolytic pathway [36]. As expected, treating L929sAhFas with anti-Fas resulted in the generation of a GSDME fragment of ~35 kDa (Fig. 1a), indicating proteolytic activation of GSDME by caspase-3 as previously reported [9, 37]. To investigate the role of GSDME in anti-Fas-mediated apoptosis, we generated *Gsdme* knockout (KO) L929sAhFas clones by CRISPR/Cas9 gene editing (Fig. 1b). Next, we investigated whether the loss of GSDME expression in *Gsdme* KO L929sAhFas clones (KOcl1 and KOcl2) affected the kinetics of the uptake of the cell-impermeable DNA-binding fluorescent dye SB during apoptosis-driven secondary necrosis (Fig. 1c). Upon anti-Fas treatment, *Gsdme* KO L929sAhFas clones (KOcl1 and KOcl2) showed a delay in the uptake of SB compared to the parental cells and *Gsdme* wild-type (WT) clones in which CRISPR/Cas9 gene editing failed to interrupt *Gsdme* (WTcl1 and WTcl2, Fig. 1c), indicating delayed plasma membrane permeabilization in absence of GSDME expression, as concluded from the SB staining. To confirm that this delay was GSDME-dependent and did not result from a clonal effect, *Gsdme* KOcl2 L929sAhFas was reconstituted with a doxycycline-inducible mGSDME construct using viral transduction, hereafter referred to as L929sAhFas iGSDME cells. Treatment of these cells with doxycycline resulted in the expression of GSDME that was cleaved to its active form upon treatment with anti-Fas (Fig. 1d). To compare the progression of apoptosis between GSDME-expressing (L929sAhFas iGSDME+) and GSDME-deficient (L929sAhFas iGSDME-) cells in more detail, we measured nuclear staining by SB and membrane surface PS exposure with Annexin V (AnnV) (Fig. 1e).

Reconstitution of GSDME expression in L929sAhFas iGSDME cells by doxycycline treatment accelerated SB-positivity upon anti-Fas treatment compared to GSDME-deficient cells (Fig. 1e-f), suggesting that the plasma membrane permeabilization kinetics are slower in cells lacking GSDME. Interestingly, upon anti-Fas treatment, both L929sAhFas iGSDME<sup>+</sup> and iGSDME<sup>-</sup> cells displayed a similar increase in membrane surface PS exposure as measured by AnnV staining (AnnV<sup>+</sup> cells, Fig. 1g). Given this similar kinetics of AnnV-positivity, the slower SB-positivity in L929sAhFas iGSDME<sup>-</sup> cells correlates with a prolonged PS single-positive stage (AnnV<sup>+</sup>/SB<sup>-</sup>, Fig. 1h). The number of AnnV<sup>+</sup>/SB<sup>-</sup> cells starts to decline in L929sAhFas iGSDME<sup>+</sup> conditions, 4 h after anti-Fas treatment, while in cells lacking GSDME a prolonged PS single-positive stage (AnnV<sup>+</sup>/SB<sup>-</sup>) can be observed (Fig. 1h). These data suggest that the initial progression of apoptotic signaling, leading to PS exposure, is not affected by GSDME expression, but GSDME is required to speed up plasma membrane permeabilization as measured by SB staining. Moreover, our results indicate that the loss of GSDME expression delays but not prevents plasma membrane permeabilization thereby suggesting that other, GSDME-independent, plasma membrane permeabilization mechanisms exist during apoptosis-driven secondary necrosis in L929sAhFas cells.

### **Gasdermin E pore formation supports influx of 10 kDa dextrans independent of plasma membrane permeabilization kinetics**

Having confirmed that GSDME expression accelerates nuclear DNA staining by SB (Fig. 1f), we next evaluated whether GSDME-dependent membrane permeabilization supports the influx of large, membrane-impermeable macromolecules as well. Texas Red-labeled dextrans with a size of 10 kDa (TR10) were used to this end, allowing convenient quantification of influx by flow cytometry (Fig. 2a). Texas Red signal was assessed in SB<sup>-</sup> and SB<sup>+</sup> cells separately, according to the zones indicated in Fig. 2b. Remarkably, treatment of L929sAhFas iGSDME cells with anti-Fas followed by incubation with TR10 and SB resulted in a TR10 single-positive population (Fig. 2b, TR10<sup>+</sup>/SB<sup>-</sup>, black arrow) and a double-positive population (Fig. 2b, TR10<sup>+</sup>/SB<sup>+</sup>), suggesting that TR10 can already enter the cells before SB stains the nuclear DNA (Fig. 2b). Unlike Fas-induced PS exposure, which happened independently of GSDME expression (Fig. 1g), TR10 tends to accumulate in twice as much SB<sup>-</sup> L929sAhFas iGSDME<sup>+</sup> cells compared to SB<sup>-</sup> cells lacking GSDME expression (Fig. 2c). This observation suggests that the influx of TR10 is enhanced by GSDME-dependent plasma membrane permeabilization in the sublytic phase, before staining by SB. Consistent with this, the TR10<sup>+</sup>/SB<sup>+</sup> population was higher in GSDME-expressing cells (Fig. 2d), which is expected as we showed that, upon anti-Fas treatment, staining by SB was accelerated in L929sAhFas iGSDME<sup>+</sup> cells (Fig. 1f).

Next, we investigated whether the GSDME-related difference observed in TR10 influx is simply the result of delayed cell death kinetics, measured by SB staining, in L929sAhFas iGSDME<sup>-</sup> or a direct consequence of the absence of the GSDME pore itself. To neutralize the difference in cell death kinetics in our results, as pointed out in the previous section (Fig. 1f), we assessed TR10 uptake in the SB<sup>-</sup> and SB<sup>+</sup> population by normalizing the number of TR10<sup>-</sup> and TR10<sup>+</sup> cells against the total number of cells in the respective populations (Fig. 2e-f). Apparently, the fraction of TR10<sup>+</sup> cells upon anti-Fas treatment in SB<sup>-</sup> L929sAhFas iGSDME<sup>-</sup> cells was limited and significantly less compared to when GSDME was present

(Fig. 2e). This suggests that GSDME pore formation itself allows the influx of TR10 before SB-mediated nuclear staining. In SB+ cells, TR10 entered L929sAhFas iGSDME- cells much more easily, pointing to other permeabilization mechanisms taking place as well during apoptosis-driven secondary necrosis (Fig. 2f). Still, TR10 entered L929sAhFas iGSDME+ cells significantly more, indicating that plasma membrane permeabilization by GSDME enhances TR10 influx. Interestingly, both in SB- (Fig. 2e) and SB+ cells (Fig. 2f), the fraction of TR10+ cells increased over time. This suggests that the longer a cell remains SB- upon anti-Fas treatment, the more cells are porated, possibly with bigger pores, thereby promoting the entrance of TR10 while cells are in the sublytic phase and are not yet stained by SB. Altogether, our results indicate that GSDME promotes faster and increased influx of TR10 in both SB- as SB+ cells during apoptosis-driven secondary necrosis.

### **Gasdermin E pore formation facilitates the influx of large dextrans in a size-dependent manner**

As TR10 is able to enter L929sAhFas iGSDME cells even when GSDME is absent, we wondered whether there is a molecular weight above which dextrans can no longer enter GSDME-deficient cells. Therefore, we examined the influx of Texas Red-labeled dextrans of 40 kDa (TR40), 70 kDa (TR70) and of 2000 kDa (TR2000) and how this is affected by GSDME expression in L929sAhFas iGSDME cells upon anti-Fas treatment. Influx of Texas Red-labeled dextrans was again assessed in both SB- and SB+ cells separately. Overall, upon 8 h (Fig. 3a) and 10 h (Fig. 3b) of treatment with anti-Fas, absence of GSDME expression significantly reduced the influx of all dextran sizes in SB- L929sAhFas iGSDME cells, while influx clearly did happen when GSDME was present, except for TR2000. Although prolonged anti-Fas treatment promoted influx of Texas Red-labeled dextrans up to 70 kDa in both L929sAhFas iGSDME+ and iGSDME- cells, this was still significantly lower in absence of GSDME (Fig. 3b). Moreover, the uptake of Texas Red-labeled dextrans in SB- cells decreased with increasing dextran size, both in the absence (10 h,  $p < 0.01$ ) and presence (8 h,  $p < 0.05$ ; 10 h,  $p < 0.01$ ) of GSDME expression (Fig. 3a-b). These observations point toward pore formation during apoptosis-driven secondary necrosis with a rather variable instead of a fixed size. These results suggest that GSDME pores formed in SB- L929sAhFas iGSDME cells allow the passage of dextrans up to at least 70 kDa while they exclude the entrance of Texas Red-labeled dextrans equal or larger than 2000 kDa. Importantly, note that the GSDME-dependent influx of Texas Red-labeled dextrans happened prior to SB staining, suggesting that GSDME membrane permeabilization during apoptosis-driven secondary necrosis does not occur concurrently with nuclear DNA staining by small SB molecules (0.4 kDa) and already happens prior to secondary necrosis.

The GSDME dependency for the influx in SB+ L929sAhFas iGSDME cells was less pronounced for TR10 after treatment with anti-Fas for 8 h (Fig. 3c), whereas after 10 h influx of sizes 10 to 70 kDa revealed to be non-significant between L929sAhFas iGSDME+ and iGSDME- cells (Fig. 3d). Nevertheless, GSDME expression clearly promoted the entrance of TR2000 in SB+ L929sAhFas iGSDME+ cells after treatment with anti-Fas for 10 h (Fig. 3d). Although this suggests that GSDME pores in SB+ cells might even favor the entrance of molecules up to 2000 kDa, most of the cells (~70 %) were still negative for TR2000. Furthermore, similar to the influx in SB- cells, influx of Texas Red-labeled dextrans significantly decreased with increasing dextran size. On average, dextran size had an overall statistical significant effect on the

influx 8 h after anti-Fas treatment in L929sAhFas iGSDME<sup>-</sup> cells (Fig. 3c,  $p < 0.001$ ) and 10 h after anti-Fas treatment in L929sAhFas iGSDME<sup>+</sup> (Fig. 3d,  $p < 0.05$ ) and iGSDME<sup>-</sup> (Fig. 3d,  $p < 0.001$ ) cells. Linear fit of the data points for TR10, TR40 and TR70 upon 8 h (Fig. 3e) and 10 h (Fig. 3f) of anti-Fas treatment, allowed us to interpolate the size of molecules that can enter 50 % of the cells (Fig. 3e-f). According to our calculations, GSDME expression would allow the uptake of molecules between 115 (8 h) and 125 kDa (10 h) in 50 % of the SB<sup>+</sup> L929sAhFas iGSDME<sup>+</sup> cells, while absence of GSDME limits the molecular size to 53 (8 h) and 87 kDa (10 h).

### **Nanoparticle-sensitized photoporation constitutes a suitable method for introducing dextrans into cells without influencing apoptosis kinetics**

Although monitoring the influx of Texas Red-labeled dextrans provided insight in the molecular weight of molecules that can enter during apoptosis-driven secondary necrosis, we aimed to evaluate whether the same conclusions are reached when monitoring the efflux of macromolecules. Monitoring efflux should better reflect the physiological situation where intracellular content like Damage Associated Molecular Patterns (DAMPs) or even cell organelles are released from dying cells. Instead of Texas Red-labeled dextrans, of which we observed that they tend to interact with intracellular constituents, we used FITC-labeled dextrans, which are inert in cells [38]. For delivery of FITC-labeled dextrans in the cytosol of L929sAhFas cells, we used nanoparticle-sensitized photoporation as an emerging intracellular delivery technique that minimally perturbs the cellular homeostasis (Fig. 4a) [23, 24, 27]. L929sAhFas cells were first incubated with cationic AuNPs, which attach to the plasma membrane. After washing away unbound AuNPs, cells were irradiated with a 5 nanosecond laser pulse ( $\lambda = 532$  nm,  $1.6$  J/cm<sup>2</sup>), resulting in the formation of transient pores in the plasma membrane through which the fluorescently labeled dextrans can diffuse into the cytosol.

First, we optimized the AuNP concentration as function of delivery efficiency and cell metabolic activity. To maximize cell loading and minimize potential cell cytotoxicity by photoporation, different AuNP concentrations ( $2, 4, 6, 8$  and  $16 \times 10^7$  AuNPs/mL) were screened using a fixed laser pulse fluence of  $1.6$  J/cm<sup>2</sup>. We observed an increase in the percentage of cells positive for FITC-labeled dextran of 10 kDa (FD10) (Fig. S1a), as measured by flow cytometry, and a decrease in metabolic activity, as measured with the CellTiter-Glo<sup>®</sup> assay (Fig. S1b), for increasing AuNP concentrations. Allowing a 30 % reduction in metabolic activity, determined by the ATP content of live cells, the optimal AuNP concentration was set at  $6 \times 10^7$  AuNPs/mL for all further experiments, in which case near 100 % of the cells are FD10 positive. In addition, we tested whether photoporation of FD10 influenced cell death kinetics of L929sAhFas cells when treated with anti-Fas. *Gsdme* WT and KOcl2 L929sAhFas cells were photoporated in the presence of FD10 and cell death kinetics, as determined by SB staining, was compared with untreated control cells. Cell death kinetic measurements of photoporated cells remained unchanged compared to the untreated control cells (Fig. S2). Based on these results, we concluded that photoporation can efficiently deliver FITC-labeled dextrans in L929sAhFas cells without influencing anti-Fas-mediated apoptosis-driven secondary necrosis.

## **Efflux of dextrans of 10 kDa occurs independently of gasdermin E expression and cell death kinetics during apoptosis-driven secondary necrosis**

Having optimized the cytosolic delivery of FD10 with nanoparticle-sensitized photoporation, we investigated the efflux of the dextrans from L929sAhFas iGSDME cells upon anti-Fas treatment, as a function of the SB signal of the cells (Fig. 4a). Following this strategy, we gated the whole cell population undergoing anti-Fas treatment into: no SB signal (SB-), a low SB signal (SB low+) and a high SB signal (SB high+) (Fig. 4b). Flow cytometry data revealed that both in presence and absence of GSDME, FD10 was released from the cells when they became positive for the SB-mediated nuclear staining (Fig. 4b-c). Interestingly, a bimodal distribution in the FITC signal was observed in cells with a low SB signal (Fig. 4c, middle panel), which was not observed in the influx experiments. This observation indicates that in the initial stage, when the nucleus of cells gets stained by SB, a part of those cells had already lost FD10 content while the other part was still clearly FD10 positive. In contrast, only a very few SB- cells were negative for FD10 (Fig. 4c, left panel), while cells with a high SB+ signal had practically all lost their dextran content (Fig. 4c, right panel). Of note, these results were observed independent of GSDME expression.

This strong heterogeneity of dextran release between SB- and SB high+ cells is confirmed when plotting the mean fluorescent intensity of FD10 relative to the untreated SB- cells (rMFI) for the SB-, SB low+ and SB high+ population, respectively (Fig. 4d-f). Note that we chose to use the rMFI to present the loss of FITC-labeled dextrans, as photoporation delivery efficiency (i.e. the percentage of FD10 positive cells) decreases with increasing dextran size [24, 39]. Only a minimal amount of FD10 content was released from SB- cells (Fig. 4d). Surprisingly, the rMFI decreased slightly but significantly more in the absence of GSDME than in GSDME-reconstituted cells, suggesting that there would be more content release over time in SB- cells when GSDME is lost. This is a counterintuitive result, which is in contrast with our influx data that pointed toward facilitated uptake of dextrans when GSDME pores are formed in SB- cells. However, referring to the prolonged stage of PS-positivity in SB- cells without GSDME expression (Fig. 1h), we hypothesize that the larger drop in rMFI in those cells can be attributed to the prolonged release of FD10-loaded apoptotic membrane blebs in cells lacking GSDME. Taken together, based on these data, we could not claim that GSDME expression facilitates the efflux of small dextrans in SB- L929SAhFas iGSDME cells upon anti-Fas treatment.

In strong contrast to the SB- population, SB high+ cells have lost almost all of their FD10 content irrespective of GSDME expression (Fig. 4f). While the SB low+ population had an intermediate rMFI level, there was no difference between GSDME-expressing and non-expressing cells (Fig. 4e). Interestingly, treating cells for longer time periods with anti-Fas resulted in a decreased rMFI of FD10 in the SB low+ population, indicating a different content release behavior of slower-dying cells. More specifically, based on these observations, it seems that cells in which SB-staining is initiated later upon anti-Fas treatment, are more likely to lose their content earlier in the dying process, while the opposite holds true for faster-dying cells.

## Efflux of dextrans is size-dependent but gasdermin E-independent during apoptosis-driven secondary necrosis

To evaluate whether the release of dextrans from anti-Fas-treated L929sAhFas iGSDME cells is size-dependent, we monitored the efflux of FITC-labeled dextrans of increasing molecular weights: 4 kDa (FD4), 40 kDa (FD40), 70 kDa (FD70), 150 kDa (FD150), 250 kDa (FD250), 500 kDa (FD500) and 2000 kDa (FD2000). Efflux in SB<sup>-</sup> cells was size independent, albeit that L929sAhFas iGSDME<sup>-</sup> cells had lost more FITC-labeled dextrans compared to L929sAhFas iGSDME<sup>+</sup> cells (Fig. 5a). This supports our previous hypothesis that dextran loss is dominated by blebbing in SB<sup>-</sup> cells, especially in the absence of GSDME. In contrast, SB<sup>high+</sup> cells have lost almost all FITC-labeled dextran content of all sizes independent of GSDME expression (Fig. 5c). Nevertheless, a slight size-dependent trend was seen, indicating less dextran release with increasing molecular weight, which was significant in the absence of GSDME expression (Fig. 5c). This size-dependent trend was more obvious in SB<sup>low+</sup> (Fig. 5b), although again only significant for GSDME-deficient cells. Together these data point towards a size-dependent but GSDME-independent release of dextrans as soon as cells start to become positive for SB. Although no clear size cut-off of the GSDME pore could be determined *via* this strategy, release of FITC-labeled dextrans in general is size-dependent during apoptosis-driven secondary necrosis. This can be concluded from the stronger release of smaller-sized dextrans in SB<sup>low+</sup> cells compared to larger-sized dextrans, which tend to be released rather at the end of permeabilization (Fig. 5a-b, Fig. S3a-b). The fact that larger-sized dextrans are less easily released as compared to smaller-sized dextrans may indicate the presence of another, GSDME-independent, plasma membrane permeabilization subroutine in SB<sup>+</sup> cells that allows the release of FITC-labeled dextrans in a size-dependent way. Of note, as limited efflux was observed in SB<sup>-</sup> cells, the subroutine promoting efflux of FITC-labeled dextrans coincided with SB staining in our cells. Importantly, as concluded from previous sections, cell death kinetics measured by SB-mediated nuclear staining is delayed in L929sAhFas iGSDME cells in the absence of GSDME expression (Fig. 1f). Therefore, one can expect that a delayed efflux of FITC-labeled dextrans is similar to the delay of influx (not corrected for cell death kinetics) in L929sAhFas iGSDME cells in absence of GSDME expression (Fig. 2c-d). Indeed, when evaluating the rMFI (relative to all untreated cells) of the complete cell population (without gating for SB signal), overall a slower efflux of FITC-labeled dextrans was observed in L929sAhFas iGSDME<sup>-</sup> cells in function of anti-Fas treatment (Fig. 5d). Although efflux of FITC-labeled dextrans through the GSDME pore seems unlikely, this observation highlights the importance of GSDME in the overall cellular release of FITC-labeled dextrans. Altogether, our results suggest that GSDME contributes to a larger set of mechanisms steering membrane permeabilization during apoptosis-driven secondary necrosis and by consequence content release.

## Discussion

Plasma membrane permeabilization following apoptosis-driven secondary necrosis has always been perceived as a non-regulated process of apoptotic cells in the absence of sufficient phagocytic cell capacity [2, 40]. Recently, it was shown that this plasma membrane permeabilization is a regulated process driven by caspase-3-mediated activation of GSDME [9]. This finding indicates that the cell can

accelerate the process of permeabilization by engaging GSDME-mediated release of intracellular content, which affects the inflammatory response [41]. Although pore formation by GSDMA3 and GSDMD has already been extensively studied [20–22], the kinetics and size characteristics of GSDME pore formation during apoptosis-driven secondary necrosis are currently unknown. Determining the degree of membrane permeabilization and identifying molecular sizes able to pass the plasma membrane upon GSDME expression may give insights in the membrane destabilizing behavior of GSDME and its role in progressing apoptotic cells toward secondary necrosis.

In the first part of this study, we showed that GSDME expression contributes to apoptosis-driven secondary necrosis in L929sAhFas cells by accelerating cell death kinetics measured by SB staining. This is consistent with the findings of Rogers *et al.* stating that GSDME is necessary for the quick progression of apoptotic cells toward secondary necrosis [9]. Additionally, we demonstrated that GSDME expression is dispensable for Fas-induced PS exposure in L929sAhFas, which is an early subroutine of apoptosis. As GSDME expression does accelerate plasma membrane permeabilization, dying cells remain longer in the PS single-positive stage in the absence of GSDME expression. The physiological consequences of these observations are currently unknown. It is tempting to speculate that prolonged exposure of eat-me signals facilitates efficient clearance of these cells. Yet, GSDME expression was shown to increase phagocytosis of tumor cells by macrophages as well as the number and cytolytic activity of tumor-infiltrating natural-killer and CD8+ T lymphocytes, thereby suppressing tumor growth [41].

In the second part of this study, we monitored the influx and efflux of dextran molecules of various sizes in L929sAhFas iGSDME cells with and without GSDME expression. Our results based on the influx of Texas Red-labeled dextrans suggest that GSDME-dependent pore-formation in the sublytic phase, before SB-mediated nuclear staining, allows the passage of molecules with sizes up to 70 kDa, while influx is reduced and delayed in the absence of GSDME expression. This is consistent with earlier reports presenting that GSDMD and GSDME pores in sublytic cells upon pyroptotic stimuli are crucial for the release of cytokines such as active IL-1 $\beta$  (18 kDa) [42–44]. Additionally, our influx-based results imply that GSDME also facilitates the uptake of larger dextrans in SB+ cells, which possibly elucidates the contribution of GSDME to final cell lysis. From our influx experiments we could estimate that GSDME-driven plasma membrane permeabilization favors the passage of molecules up until ~125 kDa. This is consistent with Evavold *et al.* reporting that macromolecules such as lactate dehydrogenase (144 kDa) were unable to pass GSDMD pores and were only released after complete cell lysis [42]. Although our results based on the influx of dextrans allowed us to conclude that GSDME favors the entrance of macromolecules, a clear cut-off size for molecules able to pass GSDME pores was not observed since we report a decrease in the uptake of Texas Red-labeled dextrans with increasing sizes. These observations might suggest that at any moment during cell death, permeabilization of plasma membranes may involve pores of different sizes that are simultaneously present in the cell population referring to the presence of alternative pore-forming molecules or less controlled pore-formation by GSDME. However, the formation of GSDME membrane pores of different sizes only seems plausible in case of a plasma membrane-destabilizing mechanism such as the carpet-like model or the formation of toroid-like pores since oligomerization and formation of discrete  $\beta$ -barrel-shaped pores are dependent on thermodynamic

stability. Nevertheless, the presence of different pore sizes could indicate that intermediate pores are formed that undergo a growing process until they reach their final stable form as shown for GSDMD pores [21, 22].

While influx experiments provided us with valuable insights regarding membrane permeabilization during apoptosis-driven secondary necrosis, we were keen to investigate the effect of this process on the efflux of FITC-labeled dextrans. Monitoring efflux should better reflect the physiological situation where intracellular content is released from dying cells. Interestingly, more intermediate dextran sizes are available with the FITC fluorophore, which could aid in drawing more precise conclusions about GSDME. We used nanoparticle-sensitized photoporation as an efficient intracellular delivery technique, of which we could show that it does not interfere with apoptosis kinetics. However, upon triggering of apoptosis-driven secondary necrosis, we did not find a contribution of GSDME to the efflux of FITC-labeled dextrans from L929sAhFas cells. In addition, SB high+ cells released almost all FITC-labeled dextrans while in our influx experiments, TR2000 failed to enter in most of the SB+ cells. These observations suggest that other, GSDME-independent, subroutines exist that allow the release of FITC-labeled dextrans. The existence of different subroutines supporting membrane permeabilization during cell death has recently been shown by Kayagaki *et al.* They report that the cell-surface protein nerve injury-induced protein 1 (NINJ1) contributes to plasma membrane permeabilization during apoptosis-driven secondary necrosis, pyroptosis and necroptosis next to GSDME, GSDMD and mixed lineage kinase domain-like (MLKL) [45]. Which subroutine is responsible for the efflux of FITC-labeled dextrans in our system remains elusive, but similar to the influx of Texas Red-labeled dextrans, efflux of FITC-labeled dextrans occurs in a size-dependent manner. As to why GSDME pores seem to exclude FITC-labeled dextrans, we cannot rule out an electrostatic effect. FITC-labeled dextrans are anionic while Texas Red-labeled dextrans are more neutral. Recently, the GSDMD pore was shown to be predominantly negatively charged preventing the passage of negatively charged cargos [46].

## Conclusions

We developed two strategies to elucidate the influence of GSDME in apoptosis-driven secondary necrosis and gained insights in the pore-forming and membrane permeabilizing behavior during this process. While a size dependency was observed for both influx and efflux of fluorescently labeled dextrans, we could only attribute an altered influx pattern to GSDME presence. Altogether, our results point to the existence of different subroutines that simultaneously regulate the passage of compounds during the cellular permeabilization process during apoptosis-driven secondary necrosis.

## Declarations

## Acknowledgements

Research in the Vandenaabeele group is supported by Flemish grants (EOS MODEL-IDI, FWO Grant 30826052), the Research Foundation Flanders (FWO) research grants (G.0E04.16N, G.0C76.18N, G.0B71.18N, G.0B96.20N), Methusalem (BOF16/MET\_V/007), iBOF20/IBF/039 ATLANTIS, Foundation against Cancer (FAF-F/2016/865, F/2020/1505, F/2020/1434), the Cancer Research Institute Ghent (CRIG) and the Ghent Gut Inflammation Group (GIGG) consortia, and the Flanders Institute for Biotechnology (VIB). E.D.S. acknowledges funding by Excellence of Science EOS MODEL-IDI (FWO Grant 30826052), Foundation against cancer (FAF-F/2016/865) and Methusalem (BOF16/MET\_V/007). K.B. gratefully acknowledges the funding by the European Research Council (ERC) under the European Union's Horizon 2020 research and innovation program (grant number 648124). J.R. and C.D.T. acknowledge funding of the Research Foundation Flanders (FWO, grant numbers 1110721N and 12S9418N respectively).

### **Competing interests**

The authors declare that there are no competing interests.

### **Availability of data and material**

The datasets generated during and/or analyzed during the current study are available from the corresponding author on reasonable request.

### **Code availability**

Not applicable.

### **Authors' contributions**

Conceptualization, E.D.S., J.R., S.S., F.B.R., K.B. and P.V.; Methodology, E.D.S., J.R., B.P., S.S., F.B.R., K.B. and P.V.; Validation, E.D.S., J.R., F.B.R., K.B. and P.V.; Formal analysis, E.D.S., J.R., B.P. and C.D.T.; Investigation, E.D.S. and J.R.; Resources, E.D.S., J.R., F.B.R., K.B. and P.V.; Data Curation, E.D.S. and J.R.; Writing - Original Draft, E.D.S. and J.R.; Writing – Review and Editing, E.D.S., J.R., B.P., C.D.T., S.S., K.R., K.O.B., W.D., F.B.R., K.B. and P.V.; Visualization, E.D.S. and J.R.; Supervision, S.S., K.R., W.D., F.B.R., K.B. and P.V.; Project administration, E.D.S. and J.R.; Funding acquisition, J.R., K.B. and P.V.

### **Ethics approval**

Not applicable.

### **Consent to participate**

Not applicable.

### **Consent for publication**

Not applicable.

## References

1. Green DR, Oguin TH, Martinez J (2016) The clearance of dying cells: table for two. *Cell Death Differ* 23:915–926. <https://doi.org/10.1038/cdd.2015.172>
2. Vanden Berghe T, Vanden, Vanlangenakker N, Parthoens E, et al (2010) Necroptosis, necrosis and secondary necrosis converge on similar cellular disintegration features. *Cell Death Differ* 17:922–930. <https://doi.org/10.1038/cdd.2009.184>
3. Boeltz S, Hagen M, Knopf J, et al (2019) Towards a pro-resolving concept in systemic lupus erythematosus. *Semin. Immunopathol.* 41:681–697
4. Nagata S (2018) Apoptosis and Clearance of Apoptotic Cells. *Annu Rev Immunol* 36:489–517. <https://doi.org/10.1146/annurev-immunol-042617-053010>
5. Sachet M, Liang YY, Oehler R (2017) The immune response to secondary necrotic cells. *Apoptosis* 22:1189–1204. <https://doi.org/10.1007/s10495-017-1413-z>
6. Ding J, Wang K, Liu W, et al (2016) Pore-forming activity and structural autoinhibition of the gasdermin family. *Nature* 535:111–116. <https://doi.org/10.1038/nature18590>
7. Kayagaki N, Stowe IB, Lee BL, et al (2015) Caspase-11 cleaves gasdermin D for non-canonical inflammasome signalling. *Nature* 526:666–671. <https://doi.org/10.1038/nature15541>
8. Shi P, Tang A, Xian L, et al (2015) Loss of conserved Gsdma3 self-regulation causes autophagy and cell death. *Biochem J* 468:325–336. <https://doi.org/10.1042/BJ20150204>
9. Rogers C, Fernandes-Alnemri T, Mayes L, et al (2017) Cleavage of DFNA5 by caspase-3 during apoptosis mediates progression to secondary necrotic/pyroptotic cell death. *Nat Commun* 8:14128. <https://doi.org/10.1038/ncomms14128>
10. Rogers C, Erkes DA, Nardone A, et al (2019) Gasdermin pores permeabilize mitochondria to augment caspase-3 activation during apoptosis and inflammasome activation. *Nat Commun* 10:1689. <https://doi.org/10.1038/s41467-019-09397-2>
11. Hou J, Zhao R, Xia W, et al (2020) PD-L1-mediated gasdermin C expression switches apoptosis to pyroptosis in cancer cells and facilitates tumour necrosis. *Nat Cell Biol* 22:1264–1275. <https://doi.org/10.1038/s41556-020-0575-z>
12. Sollberger G, Choidas A, Burn GL, et al (2018) Gasdermin D plays a vital role in the generation of neutrophil extracellular traps. *Sci Immunol* 3:1–12. <https://doi.org/10.1126/sciimmunol.aar6689>
13. Chen KW, Monteleone M, Boucher D, et al (2018) Noncanonical inflammasome signaling elicits gasdermin D-dependent neutrophil extracellular traps. *Sci Immunol* 3:eaar6676.

<https://doi.org/10.1126/sciimmunol.aar6676>

14. Shi J, Zhao Y, Wang K, et al (2015) Cleavage of GSDMD by inflammatory caspases determines pyroptotic cell death. *Nature* 526:660–665. <https://doi.org/10.1038/nature15514>
15. He W, Wan H, Hu L, et al (2015) Gasdermin D is an executor of pyroptosis and required for interleukin-1 $\beta$  secretion. *Cell Res* 25:1285–1298. <https://doi.org/10.1038/cr.2015.139>
16. Op de Beeck K, Van Camp G, Thys S, et al (2011) The DFNA5 gene, responsible for hearing loss and involved in cancer, encodes a novel apoptosis-inducing protein. *Eur J Hum Genet* 19:965–973. <https://doi.org/10.1038/ejhg.2011.63>
17. Lee BL, Mirrashidi KM, Stowe IB, et al (2018) ASC- and caspase-8-dependent apoptotic pathway diverges from the NLRC4 inflammasome in macrophages. *Sci Rep* 8:3788. <https://doi.org/10.1038/s41598-018-21998-3>
18. Tixeira R, Shi B, Parkes MAF, et al (2018) Gasdermin E Does Not Limit Apoptotic Cell Disassembly by Promoting Early Onset of Secondary Necrosis in Jurkat T Cells and THP-1 Monocytes. *Front Immunol* 9:2842. <https://doi.org/10.3389/fimmu.2018.02842>
19. Liu Z, Wang C, Yang J, et al (2019) Crystal Structures of the Full-Length Murine and Human Gasdermin D Reveal Mechanisms of Autoinhibition, Lipid Binding, and Oligomerization. *Immunity*. <https://doi.org/10.1016/J.IMMUNI.2019.04.017>
20. Ruan J, Xia S, Liu X, et al (2018) Cryo-EM structure of the gasdermin A3 membrane pore. *Nature* 557:62–67. <https://doi.org/10.1038/s41586-018-0058-6>
21. Sborgi L, Rühl S, Mulvihill E, et al (2016) GSDMD membrane pore formation constitutes the mechanism of pyroptotic cell death. *EMBO J* 35:1766–78. <https://doi.org/10.15252/embj.201694696>
22. Mulvihill E, Sborgi L, Mari SA, et al (2018) Mechanism of membrane pore formation by human gasdermin-D. *EMBO J* e98321. <https://doi.org/10.15252/embj.201798321>
23. Fraire JC, Houthaeve G, Liu J, et al (2020) Vapor nanobubble is the more reliable photothermal mechanism for inducing endosomal escape of siRNA without disturbing cell homeostasis. *J Control Release* 319:262–275. <https://doi.org/10.1016/j.jconrel.2019.12.050>
24. Xiong R, Joris F, Liang S, et al (2016) Cytosolic Delivery of Nanolabels Prevents Their Asymmetric Inheritance and Enables Extended Quantitative in Vivo Cell Imaging. *Nano Lett* 16:5975–5986. <https://doi.org/10.1021/acs.nanolett.6b01411>
25. Xiong R, Raemdonck K, Peynshaert K, et al (2014) Comparison of gold nanoparticle mediated photoporation: Vapor nanobubbles outperform direct heating for delivering macromolecules in live cells. *ACS Nano* 8:6288–6296. <https://doi.org/10.1021/nn5017742>

26. Raes L, Stremersch S, Fraire JC, et al (2020) Intracellular Delivery of mRNA in Adherent and Suspension Cells by Vapor Nanobubble Photoporation. *Nano-Micro Lett* 12:1–17. <https://doi.org/10.1007/s40820-020-00523-0>
27. Ramon J, Xiong R, De Smedt SC, et al (2021) Vapor Nanobubble-Mediated Photoporation Constitutes a Versatile Intracellular Delivery Technology. *Curr Opin Colloid Interface Sci* 54:101453. <https://doi.org/10.1016/j.cocis.2021.101453>
28. Liu J, Xiong R, Brans T, et al (2018) Repeated photoporation with graphene quantum dots enables homogeneous labeling of live cells with extrinsic markers for fluorescence microscopy. *Light Sci Appl* 7:2047–7538. <https://doi.org/10.1038/s41377-018-0048-3>
29. Wayteck L, Xiong R, Braeckmans K, et al (2017) Comparing photoporation and nucleofection for delivery of small interfering RNA to cytotoxic T cells. *J Control Release* 267:154–162. <https://doi.org/10.1016/j.jconrel.2017.08.002>
30. Lukianova-Hleb E, Hu Y, Latterini L, et al (2010) Plasmonic nanobubbles as transient vapor nanobubbles generated around plasmonic nanoparticles. *ACS Nano* 4:2109–2123. <https://doi.org/10.1021/nn1000222>
31. Hodgkins A, Farne A, Perera S, et al (2015) WGE: a CRISPR database for genome engineering. *Bioinformatics* 31:3078–3080. <https://doi.org/10.1093/bioinformatics/btv308>
32. Brinkman EK, Chen T, Amendola M, van Steensel B (2014) Easy quantitative assessment of genome editing by sequence trace decomposition. *Nucleic Acids Res* 42:e168–e168. <https://doi.org/10.1093/nar/gku936>
33. De Groote P, Grootjans S, Lippens S, et al (2016) Generation of a new Gateway-compatible inducible lentiviral vector platform allowing easy derivation of co-transduced cells. *Biotechniques* 60:252–259. <https://doi.org/10.2144/000114417>
34. Hothorn T, Bretz F, Westfall P (2008) Simultaneous inference in general parametric models. *Biometrical J.* 50:346–363
35. R Core Team (2020) R: A language and environment for statistical computing. In: *R Found. Stat. Comput.* <https://www.r-project.org/>. Accessed 10 Apr 2021
36. Vercammen D, Beyaert R, Denecker G, et al (1998) Inhibition of caspases increases the sensitivity of L929 cells to necrosis mediated by tumor necrosis factor. *J Exp Med* 187:1477–85
37. Wang Y, Gao W, Shi X, et al (2017) Chemotherapy drugs induce pyroptosis through caspase-3 cleavage of a gasdermin. *Nature* 547:99–103. <https://doi.org/10.1038/nature22393>

38. Lénárt P, Ellenberg J (2006) Monitoring the permeability of the nuclear envelope during the cell cycle. *Methods* 38:17–24. <https://doi.org/10.1016/j.ymeth.2005.07.010>
39. Raes L, Van Hecke C, Michiels J, et al (2019) Gold Nanoparticle-Mediated Photoporation Enables Delivery of Macromolecules over a Wide Range of Molecular Weights in Human CD4+ T Cells. *Crystals* 9:411. <https://doi.org/10.3390/cryst9080411>
40. Galluzzi L, Kroemer G (2017) Secondary Necrosis: Accidental No More. *Trends in Cancer* 3:1–2. <https://doi.org/10.1016/J.TRECAN.2016.12.001>
41. Zhang Z, Zhang Y, Xia S, et al (2020) Gasdermin E suppresses tumour growth by activating anti-tumour immunity. *Nature* 579:1–6. <https://doi.org/10.1038/s41586-020-2071-9>
42. Evavold CL, Ruan J, Tan Y, et al (2018) The Pore-Forming Protein Gasdermin D Regulates Interleukin-1 Secretion from Living Macrophages. *Immunity* 48:35-44.e6. <https://doi.org/10.1016/J.IMMUNI.2017.11.013>
43. Heilig R, Dick MS, Sborgi L, et al (2018) The Gasdermin-D pore acts as a conduit for IL-1 $\beta$  secretion in mice. *Eur J Immunol* 48:584–592. <https://doi.org/10.1002/eji.201747404>
44. Zhou B, Abbott DW (2021) Gasdermin E permits interleukin-1 beta release in distinct sublytic and pyroptotic phases. *Cell Rep* 35:108998. <https://doi.org/10.1016/j.celrep.2021.108998>
45. Kayagaki N, Kornfeld OS, Lee BL, et al (2021) NINJ1 mediates plasma membrane rupture during lytic cell death. *Nature* 1–8. <https://doi.org/10.1038/s41586-021-03218-7>
46. Xia S, Zhang Z, Magupalli VG, et al (2021) Gasdermin D pore structure reveals preferential release of mature interleukin-1. *Nature*. <https://doi.org/10.1038/s41586-021-03478-3>

## Figures

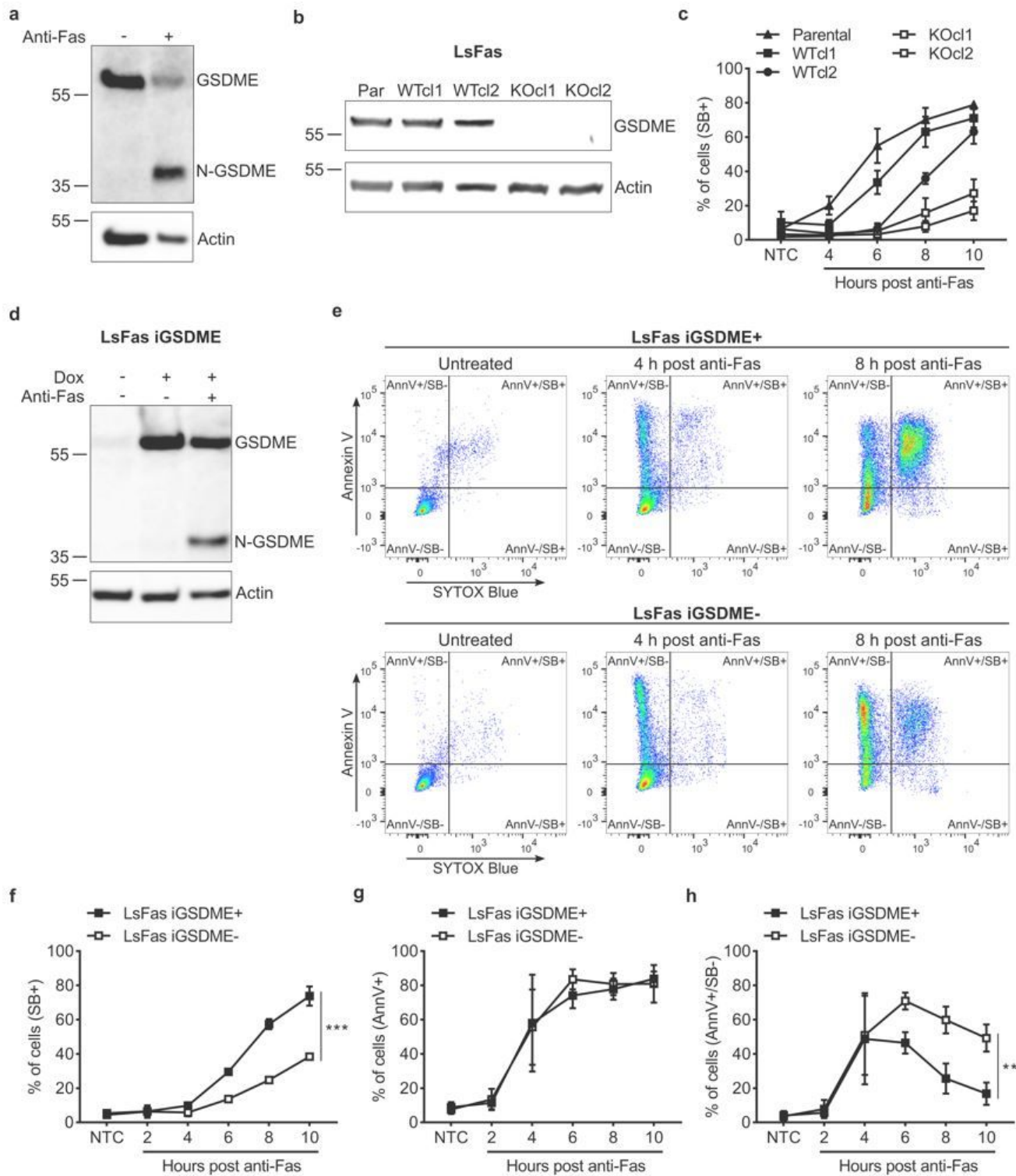


**Figure 1**

Impact of GSDME expression on apoptosis-driven secondary necrosis in L929sAhFas cells. a Expression and proteolytic cleavage of GSDME in L929sAhFas upon anti-Fas treatment. b Expression of GSDME in different L929sAhFas clones upon CRISPR/Cas 9 gene editing. c Cell death kinetics of parental, Gsdme WT and KO L929sAhFas clones measured by SB staining via flow cytometry. d Expression of GSDME in L929sAhFas iGSDME cells upon doxycycline treatment. Subsequent treatment with agonistic anti-Fas

antibodies promotes the generation of the active 35 kDa N-terminal fragment (N-GSDME). e-h Flow cytometry analysis of L929sAhFas iGSDME cells with (L929sAhFas iGSDME+) or without (L929sAhFas iGSDME-) doxycycline-induced GSDME expression during apoptosis-driven secondary necrosis. e Representative flow cytometry dot plots after 4 h or 8 h treatment with anti-Fas. f Levels of secondary necrotic (SB+) cells, g cells exposing PS (AnnV+) and h PS single-positive (AnnV+/SB-) cells in L929sAhFas iGSDME cells stimulated with anti-Fas. AnnV, Annexin V; Dox, doxycycline; GSDME, gasdermin E; KO, knockout; LsFas, L929sAhFas; NTC, non-treatment control; Par, parental; SB, SYTOX Blue; WT, wild-type

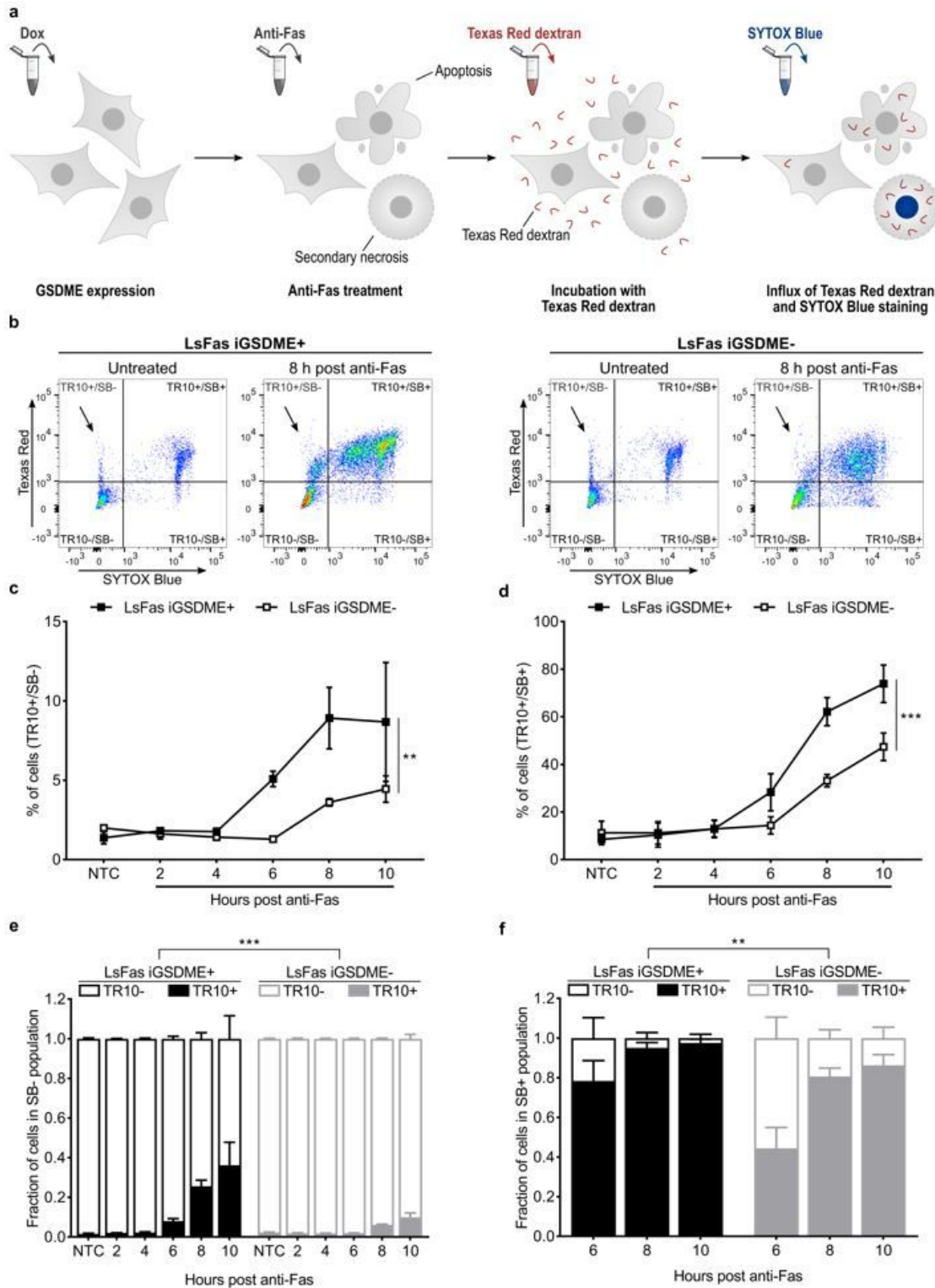


**Figure 2**

Monitoring of Texas Red-labeled dextran 10 kDa (TR10) influx in L929sAhFas iGSDME cells during apoptosis-driven secondary necrosis. **a** Principle of Texas Red-labeled dextran staining of L929sAhFas iGSDME cells. **b-f** Flow cytometry analysis of L929sAhFas iGSDME cells with (L929sAhFas iGSDME+) and without (L929sAhFas iGSDME-) doxycycline-induced GSDME expression during apoptosis-driven secondary necrosis. **b** Representative plots of L929sAhFas iGSDME cells untreated and after treatment

with anti-Fas for 8 h. c Levels of Texas Red single-positive cells (TR10+/SB-) in L929sAhFas iGSDME cells upon anti-Fas treatment. d Levels of Texas Red and SB double-positive (TR10+/SB+) cells in L929sAhFas iGSDME cells upon anti-Fas treatment. e Fraction of Texas Red positive (TR10+) and Texas Red negative (TR10-) cells in the SB- population. f Fraction of Texas Red positive (TR10+) and Texas Red negative (TR10-) cells in SB+ population. Dox, doxycycline; GSDME, gasdermin E; LsFas, L929sAhFas; SB, SYTOX Blue; NTC, non-treatment control; TR, Texas Red

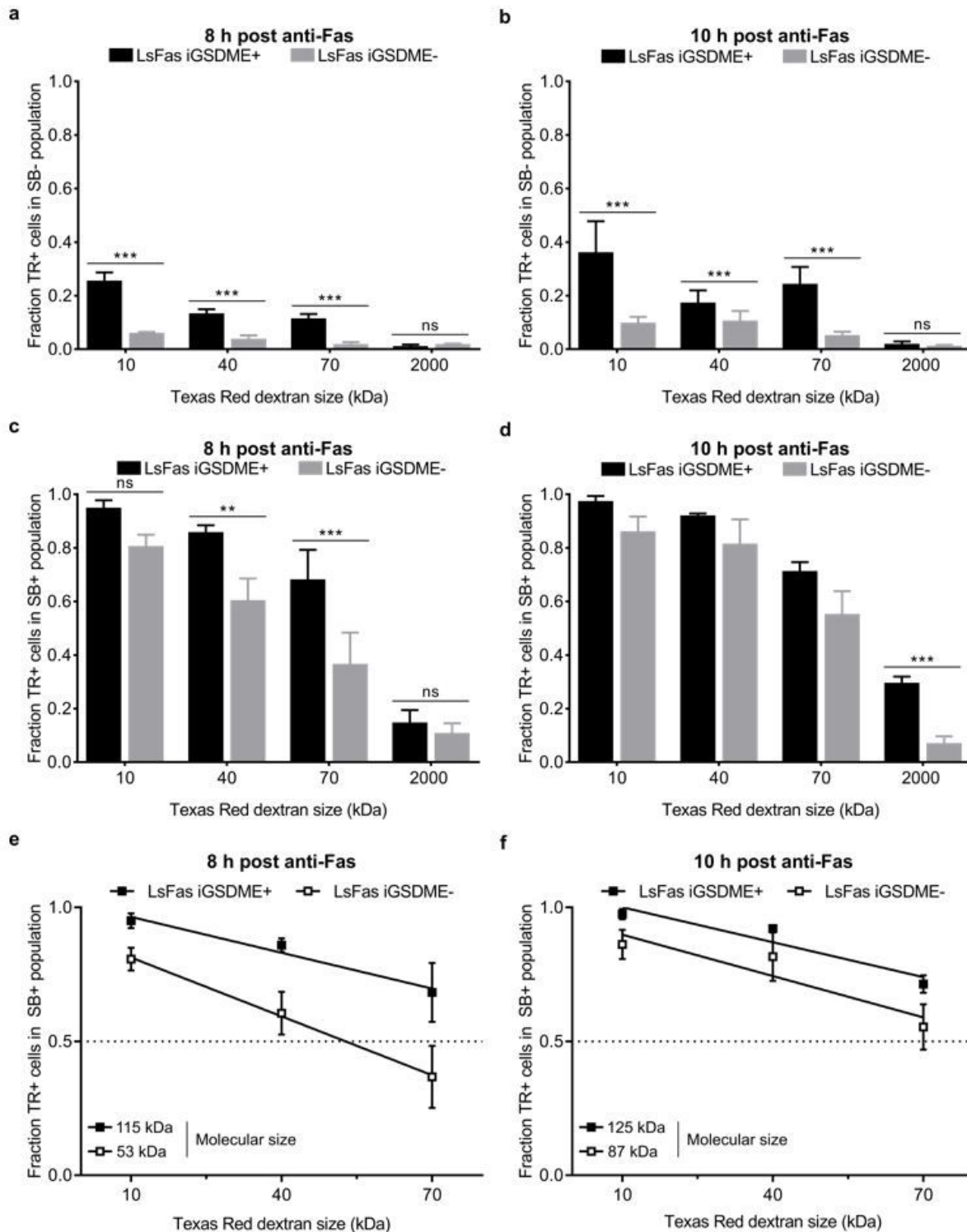
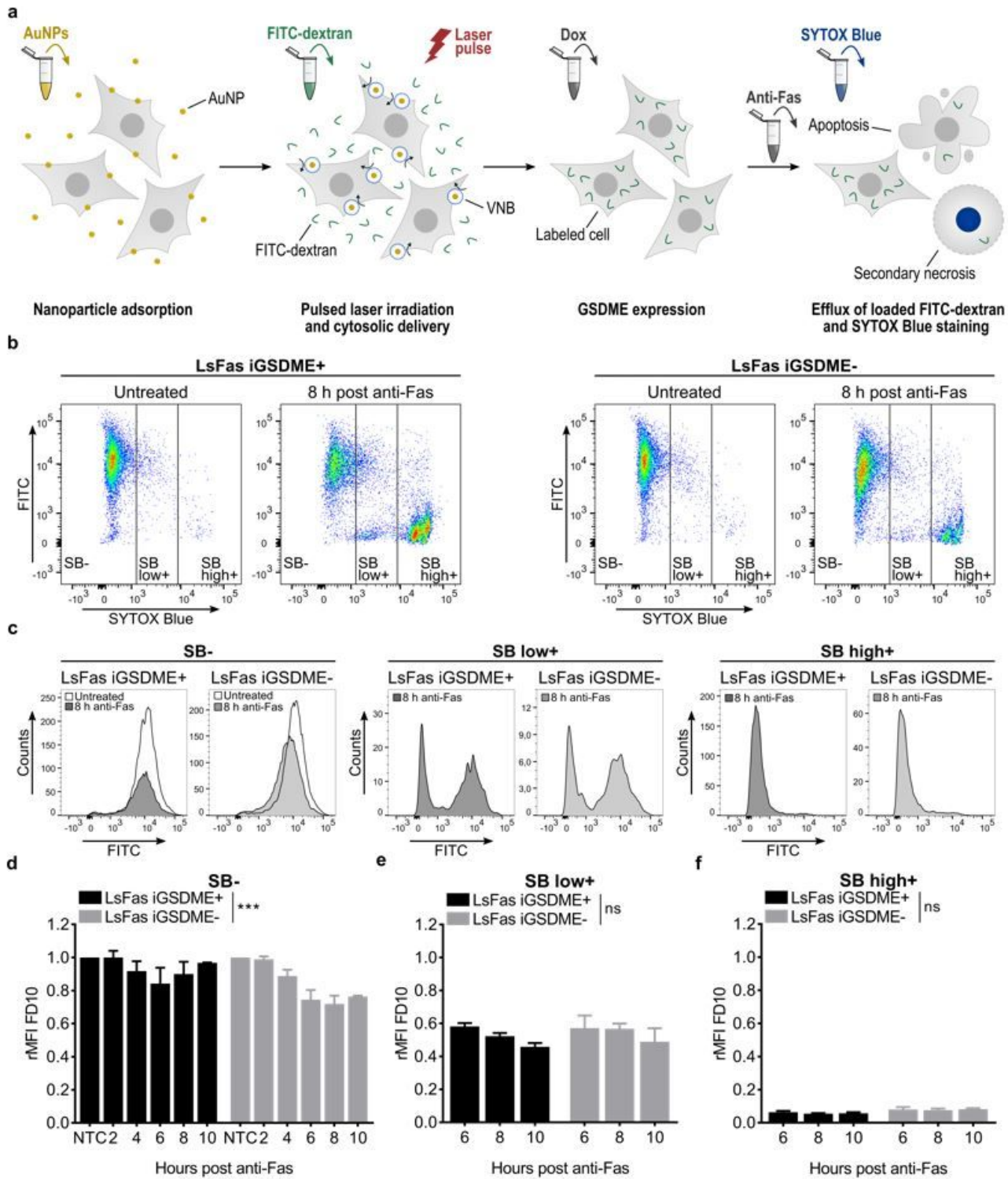


Figure 3

Influx of Texas Red-labeled dextrans of 10 kDa (TR10), 40 kDa (TR40), 70 kDa (TR70) and 2000 kDa (TR2000) in L929sAhFas iGSDME during apoptosis-driven secondary necrosis. a-f Flow cytometry analysis of Texas Red-labeled dextran uptake in L929sAhFas iGSDME cells with (L929sAhFas iGSDME+) and without (L929sAhFas iGSDME-) doxycycline-induced GSDME expression after 8 h and 10 h treatment with anti-Fas. a-b Fraction of the SB- population that is positive for various sizes of Texas Red-labeled dextrans. c-d Fraction of the SB+ population that is positive for various sizes of Texas Red-labeled dextrans. e-f Linear fit of data points for the fractions of the SB+ population positive for TR10, TR40 and TR70. Intersection of this line with the dotted line provides a rough estimation of molecular sizes that can enter 50 % of the SB+ population. LsFas, L929sAhFas; SB, SYTOX Blue; TR, Texas Red



**Figure 4**

Efflux of FITC-labeled dextrans 10kDa (FD10) from L929sAhFas iGSDME cells during apoptosis-driven secondary necrosis. **a** Principle of monitoring efflux of FITC-labeled dextrans after photoporation-based dextran loading. **b-f** Flow cytometry analysis of FD10 release in L929sAhFas iGSDME with (L929sAhFas iGSDME+) and without (L929sAhFas iGSDME-) doxycycline-induced GSDME expression when stimulated with anti-Fas. **b** Scatter plots of L929sAhFas iGSDME in presence (left) and absence (right) of GSDME

expression untreated and after 8 h treatment with anti-Fas. c Histogram plots representing the distribution of the FD10 signal in the three zones of SB staining: SB- (left), SB low+ (middle) and SB high+ (right). d Graph representing the mean fluorescent intensity of FD10 in the SB- population relative to the untreated SB- cells (rMFI) as a function of anti-Fas treatment. e Graph representing the mean fluorescent intensity of FD10 in the SB low+ population relative to the untreated SB- cells (rMFI) in function of anti-Fas treatment. f Graph representing the mean fluorescent intensity of the SB high+ population relative to the untreated SB- cells (rMFI) as a function of anti-Fas treatment. AuNP, gold nanoparticle; Dox, doxycycline; FD, FITC-dextran; GSDME, gasdermin E; LsFas, L929sAhFas; NTC, non-treatment control; SB, SYTOX Blue; VNB, vapor nanobubble

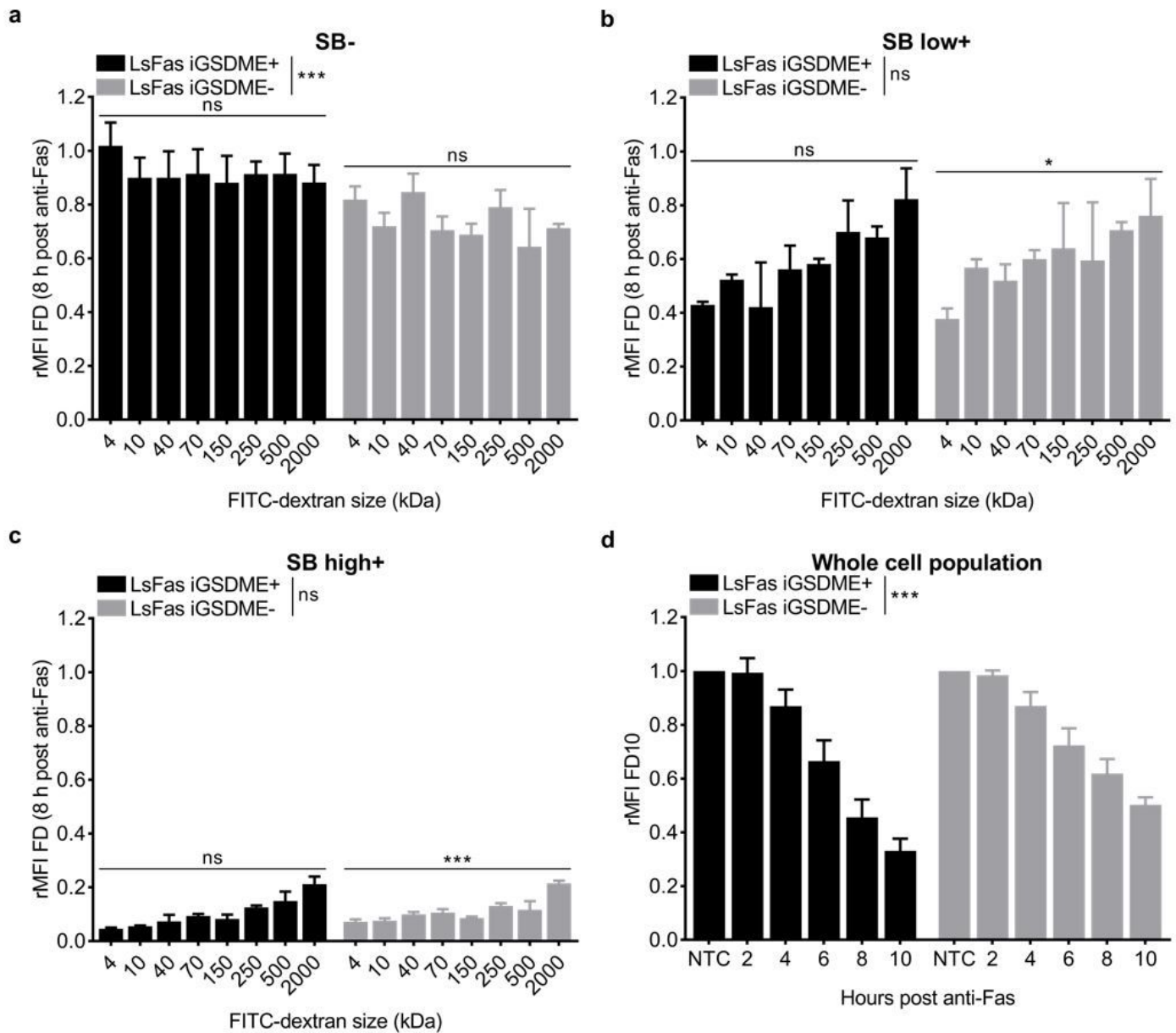


Figure 5

Efflux of FITC-labeled dextrans of different sizes from L929sAhFas iGSDME cells during apoptosis-driven secondary necrosis. a-d Flow cytometry analysis of FITC-labeled dextran release in L929sAhFas iGSDME cells with (L929sAhFas iGSDME+) and without (L929sAhFas iGSDME-) doxycycline-induced GSDME expression upon treatment with anti-Fas. a-c Graphs representing the mean fluorescent intensity relative to the untreated SB- cells (rMFI) for increasing sizes of FITC-labeled dextrans a in the SB- population, b in the SB low+ population and c in the SB high+ population after 8 h treatment with anti-Fas. d Graph representing the mean fluorescent intensity relative to the untreated cells (rMFI) for the whole cell population in function of anti-Fas exposure time. FD, FITC-labeled dextran, LsFas, L929sAhFas, NTC, non-treatment control

## Supplementary Files

This is a list of supplementary files associated with this preprint. Click to download.

- [DeSchutterRamonSupplementaryfile.pdf](#)